

Hasan Alatrash

Pore-network extraction from micro- Computed tomography images

1. Introduction

Computed tomography (CT) imaging is also known as "CAT scanning" (Computed Axial Tomography) X-Ray tomography and micro-CT. Tomography is from the Greek word "tomos" meaning "slice" or "section" and "graphia" meaning "describing". CT was invented in 1972 by British engineer Godfrey Hounsfield of EMI laboratories, England and by Allan Cormack physicist Tufts University, Massachusetts. Hounsfield and Cormack received Nobel Prize in Physiology and Medicine for 1979 for their contributions to medicine and science.

The possibility of its use in geology and engineering was soon recognized, resulting in large numbers of publications from the early 1980s onwards. Early applications include studies in the fields of soil science [1, 2], meteoritics [3], petroleum geology [4], paleontology [5], and sedimentology [6]

X-Ray tomography has become an interesting research technique, first demonstrated by Wellington [7]. Since then, the world's oil industry has used the micro-CT method as an effective tool for analyzing drilling cores, providing non-destructive rock testing and imaging of their internal structures, with particular emphasis on the nature of the pore structure. X-Ray computer micro-tomography generates a three-dimensional image of the pore space of the rock sample to be analyzed, allowing for accurate measurement and analysis of the spatial distribution of the pores [8]. Based on the results of micro-CT research we can get, among others information on porosity (volume, structure, location, pore size), number and length of pore channels and connections between them, as well as the structure of the pore network and their effect on permeability [8]. In geosciences the CT-based technique has been used in a wide range and it is continuously growing as an analytical tool. This emerging new technology provides a direct characterization of multi-modal pore size distributions and allows to predict flow properties and the productibility of a complex reservoir [9].

2. Essential of computed tomography

Micro-computed tomography or μ -CT is a non-destructive method which can be used to visualize the internal structure of a study object. It can be used for making three-dimensional reconstruction of the variation of attenuation through the object of study, the data obtained from this technique is digitized making it suitable for quantitative analysis. The X-ray CT consists of three basic elements in which the main components are:

- X-ray source
- An object that is irradiated with an x-ray
- Detector that measures the attenuated X-rays as a 2D projection image.

In the micro-tomography three steps are required: data acquisition, projection, reconstruction and 3D image visualization to move from the real object to its spatial computer image. Data acquisition consists of correctly placing the sample in the holder using one of the available fixing elements. It is very important that the axis of rotation of the sample coincide the axis of rotation of the handle, as this will give the greatest possible magnification for a given sample. Once the required position has been determined, the sample should be in the field of vision during 360° rotation. The next step is setting the appropriate scanning parameters (energy and radiation intensity and exposure time). These parameters can be used to set the contrast of the image. It is important that the image is not overwhelmed with white. The sample table is rotated every 1° in the 180° range sometimes 360° range. During the measurement, the sample is X-Rayed (the differences in absorption properties of the materials, depending on the composition of the mineral). Measurement data is collected in computer memory. In the reconstruction phase a complete 3D structure of the object will be produced, where the attenuated X-rays that are measured by the detectors will be stored in the computer memory as a 2D projection image, the series of X-ray projection images is then computed into cross-sectional images through the computational process called reconstruction [9] See figure 1 for illustration.

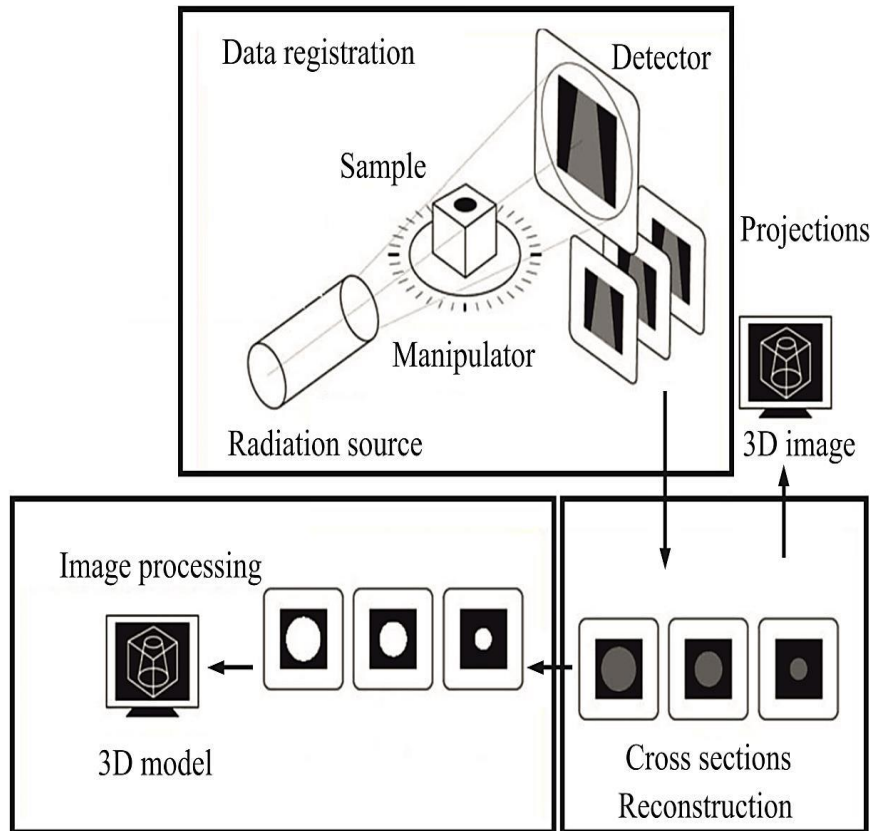


Figure 1

Working principle of CT scanners. The X-rays are generated in the source, travel through the object where they are attenuated, and are then captured by the detectors, detector that measures the attenuated X-rays as a 2D projection image then computed into cross-sectional images through the computational process. From [8]

The x-ray attenuation measured in each volume of a CT image is a linear attenuation coefficient as defined by Beer's law:

$$\frac{I}{I_0} = \exp^{-\mu h} \quad \text{Eq(1)}$$

Where:

I_0 : is the incident X-ray intensity

I : is the intensity of remaining X-ray passes through a thickness h of homogeneous sample,

μ : is the linear attenuation coefficient

2.1 X-ray source:

The important variables that determine how effective an X-ray source will be for a particular task is the size of the focal spot, the spectrum of X-ray energies generated, and the X-ray intensity [10]. The focal-spot size partially defines the potential spatial resolution of a CT system by determining the number of possible source–detector paths that can intersect a given point in the object being scanned. The more source–detector paths are, the more blurring of features will be [10]. The energy spectrum defines the penetrative ability of the X-rays, as well as their expected relative attenuation as they pass through materials of different density. Higher-energy X-rays penetrate more effectively than lower-energy ones, but are less sensitive to changes in material density and composition [10]. The X-ray intensity directly affects the signal-to-noise ratio and thus image clarity. Higher intensities improve the underlying counting statistics, but often require a larger focal spot. The energy spectrum generated is usually described in terms of the peak X-ray energy (keV or MeV), but actually consists of a continuum, in which the level with maximum intensity is typically less than half of the peak [7] Figure 2. The total “effective” energy spectrum is determined by a number of factors in addition to the energy input of the X-ray source itself, including auto-filtering both by absorption of photons generated beneath the surface of a thick target and by passage through the tube exit port [11]; other beam filtration introduced to selectively remove low-energy X-rays; beam hardening in the object being scanned; and the relative efficiency of the detectors to different energies [10]. Changes in the X-ray spectrum caused by passage through an object can lead to a variety of scanning artifacts unless efforts are made to compensate them [10].

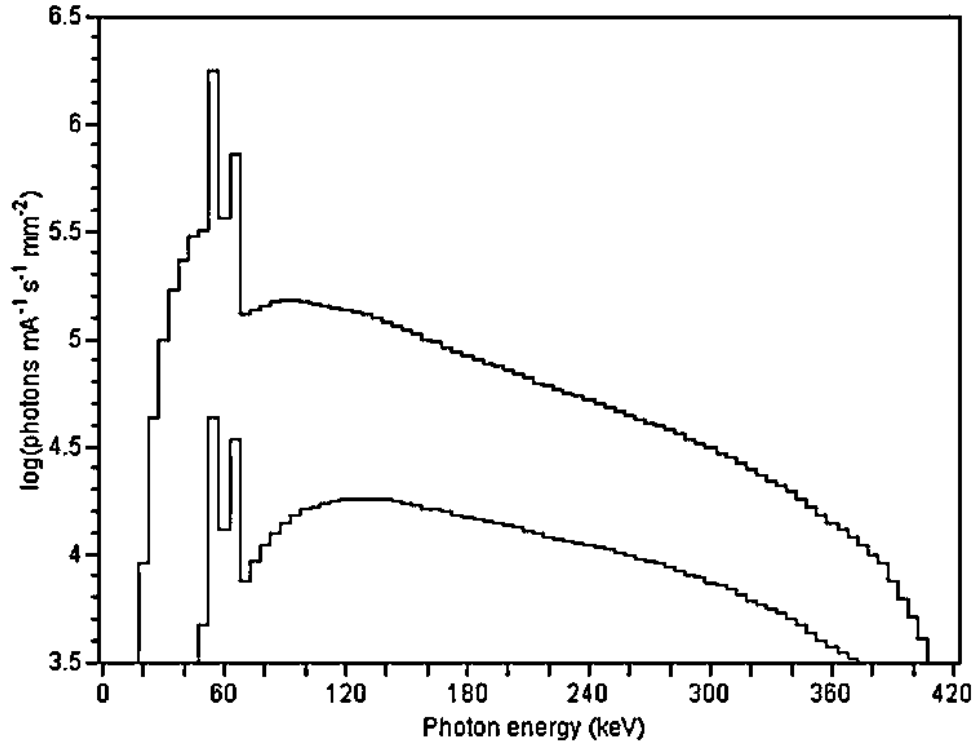


Figure 2

Theoretical energy spectra for 420-kV X-ray source with tungsten target, calculated combining

5-keV intervals. Spectra consist of continuous Brems strahlung and characteristic K- series peaks at 57–59 and 67–69 keV. Upper spectrum is modified only by inherent beam filtration by 3mm of aluminum at tube exit port. Mean X-ray energy is 114 keV. Lower curve represents spectrum that has also passed through 5 cm of quartz. Preferential attenuation of low-energy X-rays causes average energy to rise to 178 keV. From [7]

2.2 X-ray attenuation

As the X-rays pass through the object being scanned, the signal is attenuated by scattering and absorption. The basic equation for attenuation of a monoenergetic beam through a homogeneous material is the Beer's Law equation (1). If the scan object is composed of a number of different materials, the equation becomes:

$$I = I_0 \exp[\sum_i -u_i x_i] \quad \text{Eq(2)}$$

Most reconstruction strategies solve Eq. (2), insofar as they assign a single value to each pixel rather than some energy-dependent range [10].

There are three dominant physical processes responsible for attenuation of an X-ray signal: photoelectric absorption, Compton scattering, and pair production illustrated in Figure 3. Photoelectric absorption occurs when the total energy of an incoming X-ray photon is transferred to an inner electron, causing the electron to be ejected. In Compton scattering, the incoming photon interacts with an outer electron, ejecting the electron and losing only a part of its own energy, after that it is deflected in a different direction. In pair production, the photon interacts with a nucleus and is transformed into a positron-electron pair, with any excess photon energy transferred into kinetic energy in the particles produced. In general, for geological materials, the photoelectric effect is the dominant attenuation mechanism at low X-ray energies, up to approximately 50–100 keV. Compton scatter is dominant at higher energies up to 5– 10 MeV, after which pair production predominates. Thus, unless higher-energy sources are used, only photoelectric absorption and Compton scattering need to be considered [10] The best way to gain insight into what one might expect when scanning a geological sample is to plot the linear attenuation coefficients of the component materials over the range of the available X-ray spectrum. These values can be calculated by combining experimental results for atomic species [12]. Mass attenuation coefficients must be multiplied by mass density to determine linear attenuation coefficients [10]. To illustrate, Figure 4 shows curves for four minerals: quartz, orthoclase, calcite, and almandine garnet. Quartz and orthoclase are very similar in mass density (2.65 g/cm³ vs. 2.59 g/cm³), but at low energy their attenuation coefficients are quite different because of the presence of relatively high-Z (High atomic number) potassium in the feldspar. With rising X-ray energy, their attenuation coefficients converge, and at approximately 125 keV they cross; and above ~125 keV quartz is slightly (but probably indistinguishably) more attenuating, owing to its higher density. Thus, one would expect that these two minerals could be differentiated in CT imagery if the mean X-ray energy used is low enough, but at higher energies they would be nearly indistinguishable Figure 5.

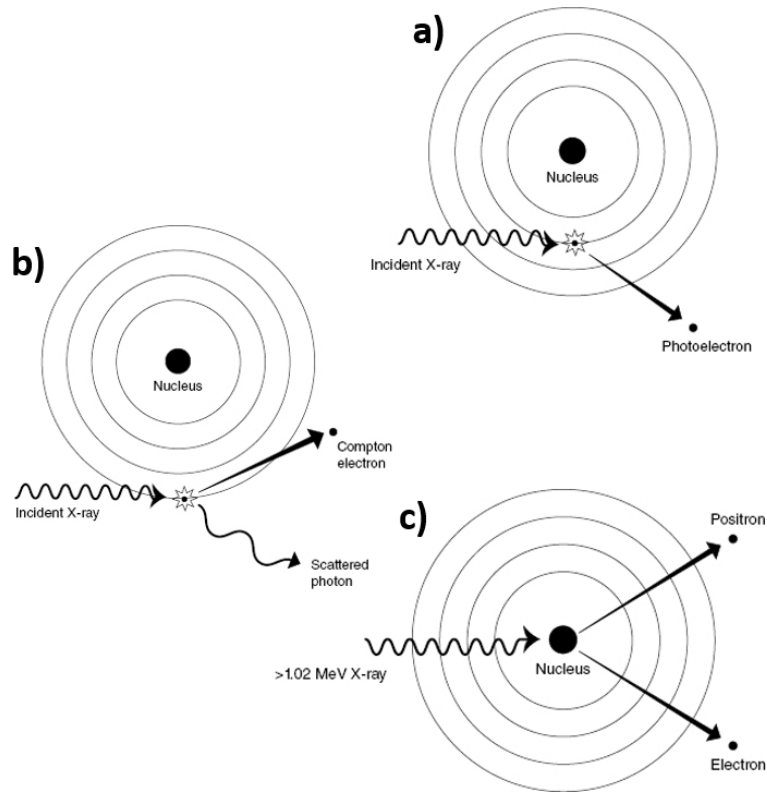


Figure 3

The three dominant physical processes responsible for attenuation of an X-ray signal: a) photoelectric absorption, b) Compton scattering, and c) pair production

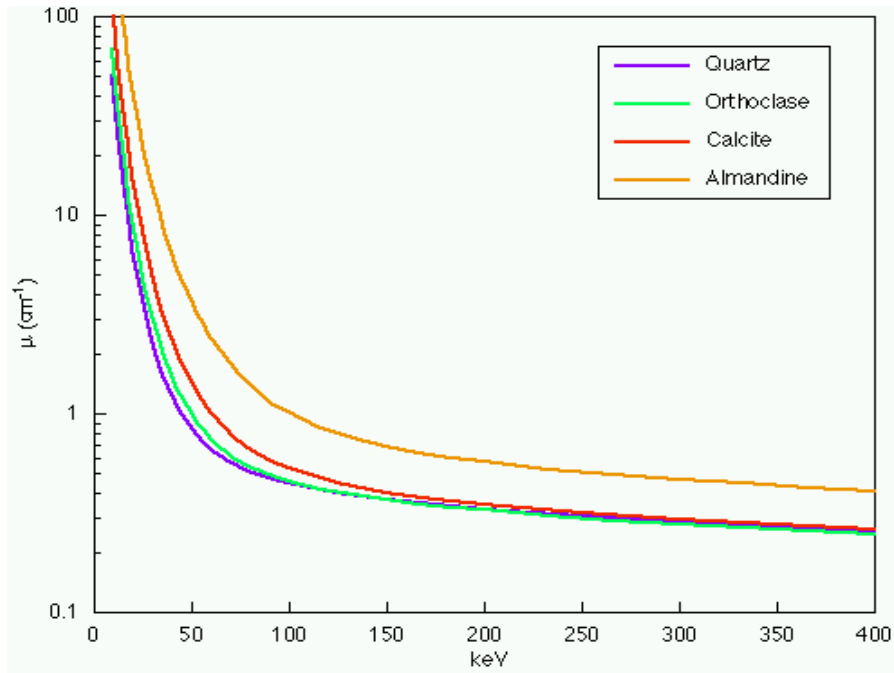


Figure 4

Linear attenuation coefficient as function of X-ray energy for four rock-forming minerals. Such

curves, when combined with the X-ray spectrum utilized for scanning (figure 2), allow prediction of the ability to differentiate between minerals in CT images. From [10]

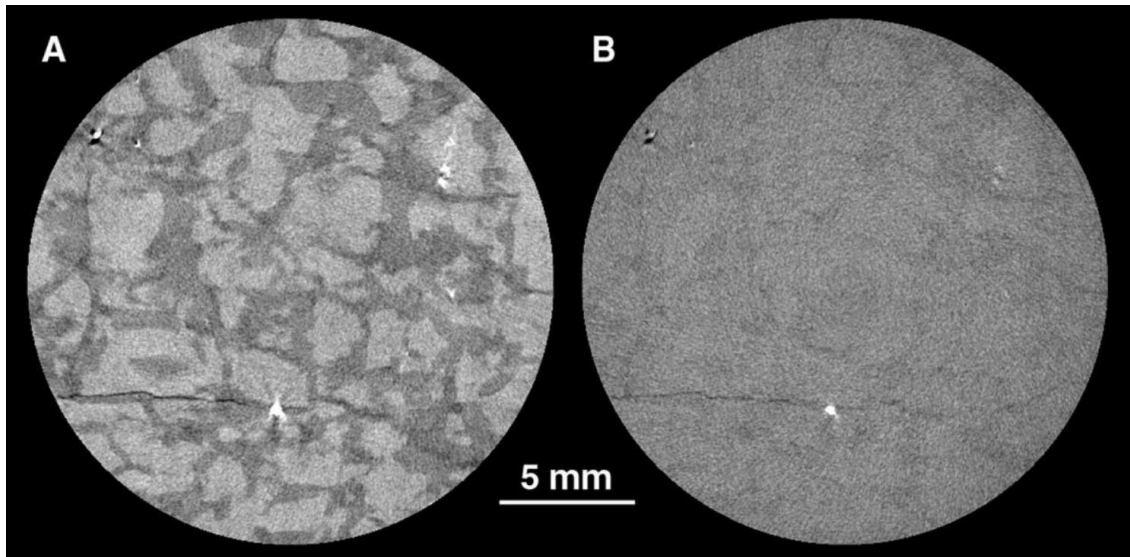


Figure 5

Core of graphic granite quartz orthoclase and mica imaged at various energy conditions. Field of view diameter for each image is 22mm, and slice thickness is 100 mm. Scan (A) was created using X-ray energy of 100keV and no beam filtration; scan (B) was acquired with X-ray energy of 200keV and 1/800 brass filter. Both scans employed “self-wedge” calibration. From [10]

2.3 X-ray detectors

Detectors for CT scanners make use of scintillating materials in which incoming X-rays produce flashes of light that are counted. Detectors influence image quality through their size and quantity, and through their efficiency in detecting the energy spectrum generated by the source. The size of an individual detector determines the amount of an object that is averaged into a single intensity reading, while the number of detectors determines how much data can be gathered simultaneously [10]. In third-generation scanning, the number of detectors also defines the degree of resolution possible in a single view, and thus in an image overall.

3. Acquisition of CT data and digital image processing

Definition of an image and image histogram. An image is a two-dimensional array of values, much like a matrix. In the case of a grayscale image, the values are scalars indicating the intensity of each pixel, for an 8-bit grayscale image, 0 represents black and 255 represents white. In an image processing context, the histogram of an image normally refers to a histogram of the pixel intensity values. This histogram is a graph showing the number of pixels in an image at each different intensity value found in that image. For an 8-bit grayscale image there are 256 different possible intensities, and so the histogram will graphically display 256 numbers showing the distribution of pixels amongst those grayscale values. In Figure 6 an example of four basic image types and their

corresponding histogram. The field of digital image processing refers to processing digital images by means of a digital computer. The diagram of image processing is shown in Figure 7. This diagram does not imply that every process is applied to an image, rather, the intention is to convey an idea of all the methodologies that can be applied to images for different purposes and possibly with different objective [13]. Image processing workflow is as follows:

- Image acquisition is the first process in image processing which includes sample preparation, calibration, scaling and reconstruction.

- Image enhancement is the process of manipulating an image so that the result is more suitable than the original for a specific application [13].

- Image restoration is an area that also deals with improving the appearance of an image. However, unlike enhancement, which is subjective, image restoration is objective, in the sense that restoration techniques tend to be based on mathematical or probabilistic models of image degradation. Enhancement, on the other hand, is based on human subjective preferences regarding what constitutes a “good” enhancement result [13].

- Wavelets are the foundation for representing images in various degrees of resolution.

- Compression, as the name implies, deals with techniques for reducing the storage required to save an image, or the bandwidth required to transmit it.

- Morphological processing deals with tools for extracting image components that are useful in the representation and description of the shape.

- Segmentation procedures partition an image into its constituent parts or objects. In general, autonomous segmentation is one of the most difficult tasks in digital image processing [13]. A rugged segmentation procedure brings the process a long way toward successful solution of imaging problems that require objects to be identified individually. On the other hand, weak or erratic segmentation algorithms almost always guarantee eventual failure. In general, the more accurate the segmentation, the more likely recognition is to succeed [13]

- Representation and description almost always follow the output of a segmentation stage, which usually is raw pixel data, constituting the region of interest.

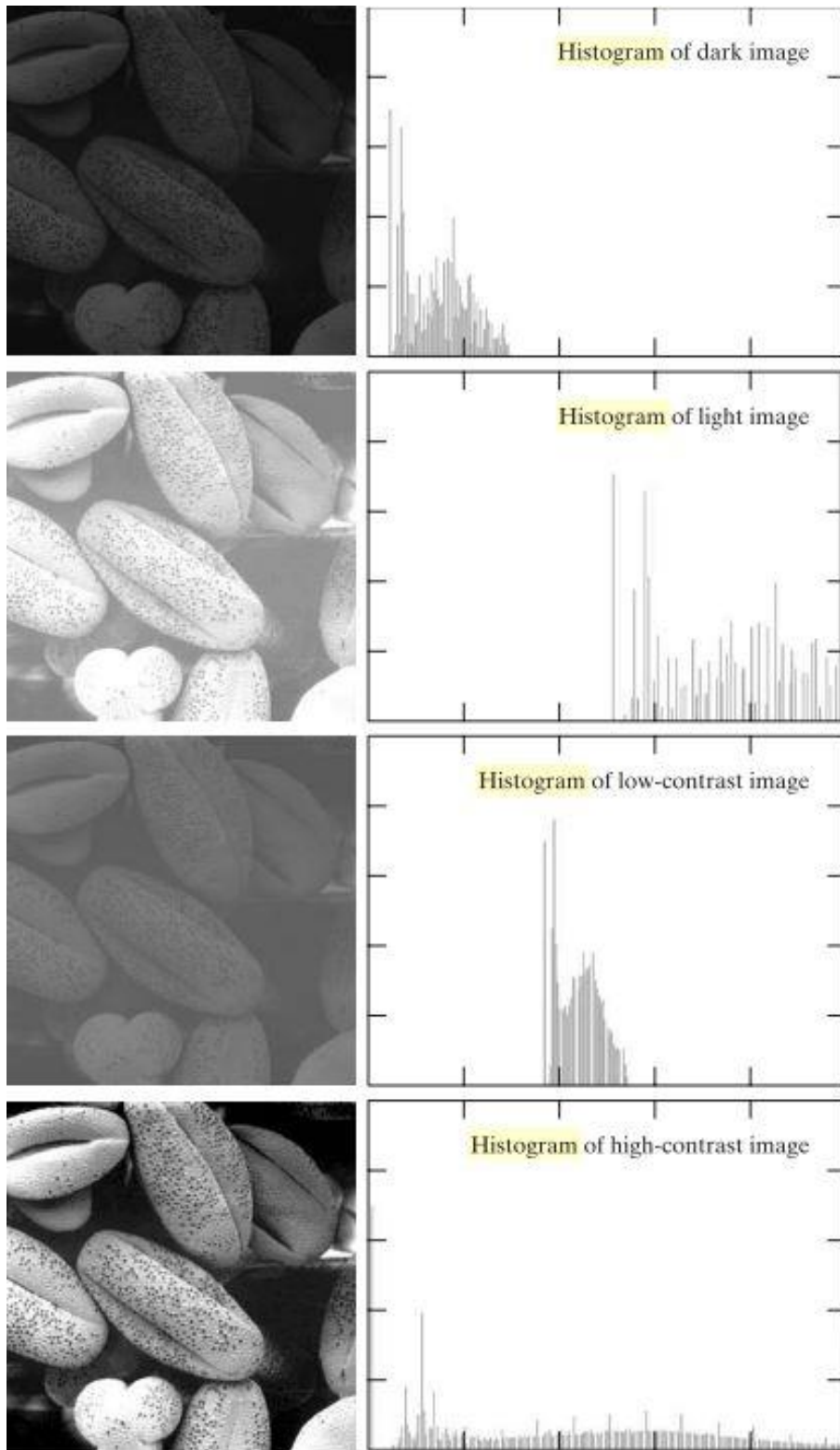


Figure 6

Four basic image types: dark, light, low contrast, high contrast, and their corresponding histograms. From [13]

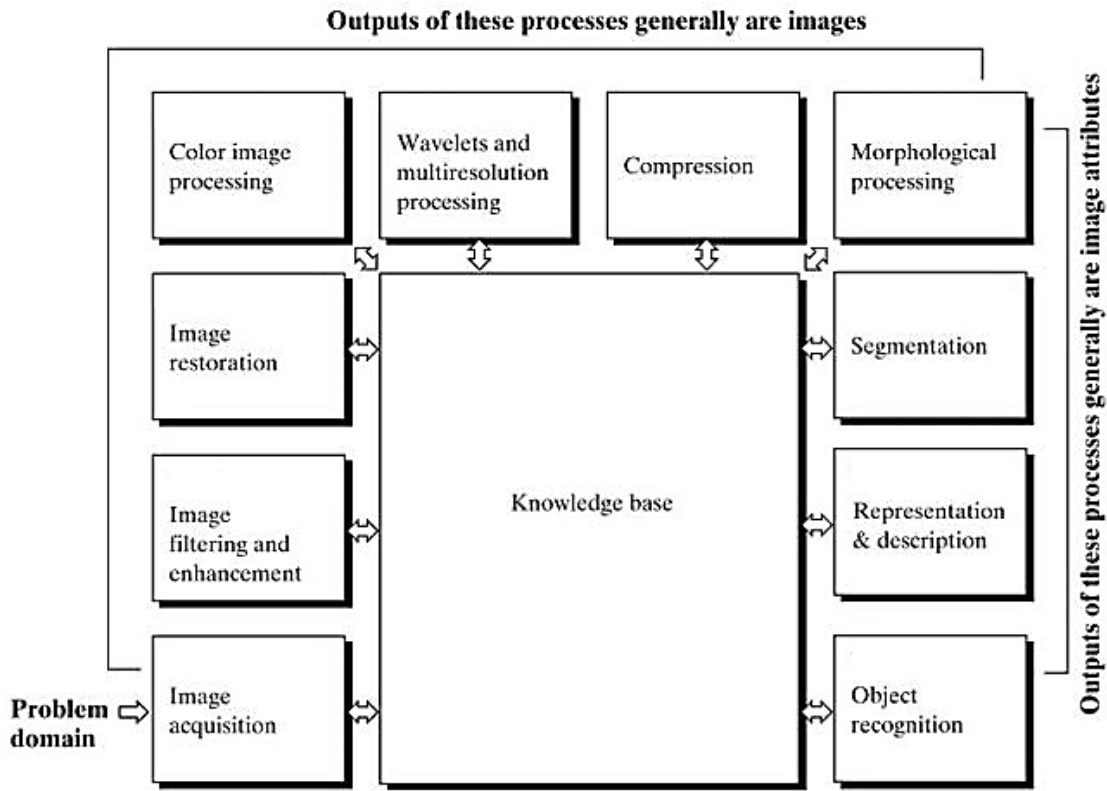


Figure 7

The diagram of image processing. From [13]

3.1 Sample preparation

Strictly speaking, the only preparation that is absolutely necessary for CT scanning is to ensure that the object fits inside the field of view and that it does not move during the scan. Because the full scan field for CT is a cylinder (i.e., a stack of circular fields of view), the most efficient geometry to scan is also a cylinder. Thus, when possible it is often advantageous to have the object take on a cylindrical geometry, either by using a coring drill or drill press to obtain a cylindrical subset of the material being scanned, or by packing the object in a cylindrical container with either X-ray-transparent filler or with material of similar density. For some applications the sample can also be treated to enhance the contrasts that are visible. Examples have included injecting soils and reservoir rocks with Sodium iodide (NaI-laced) fluids to reveal fluid-flow characteristics [14]. Injecting sandstones with woods metal (a very dense metal and absorbs energy, so it is also used as a protective shield in radiotherapy) to map out the fine-scale permeability [14].

3.2 Calibration:

The two principal signal calibrations are offset and gain, which determine the detector readings with X-rays off, and with X-rays on at scanning conditions, respectively [10]. An additional signal calibration, called a wedge, used on some third-generation systems consists of acquiring X-rays as

they pass through a calibration material over a 360° rotation. The offset-corrected average detector reading is then used as the baseline from which all data are subtracted. If the calibration material is air, the wedge is equivalent to a gain calibration. A typical non-air wedge is a cylinder of material with attenuation properties similar to those of the scan object. Such a wedge can provide automatic corrections for both beam hardening and ring artifacts [10] (described later), and can allow utilization of high X-ray intensities that would saturate the detectors during a typical gain calibration. Although widely employed in medical systems, which use phantoms of water or water-equivalent plastic to approximate the attenuating properties of tissue, the wedge calibration is relatively uncommon in industrial praxis.

3.3 Image reconstruction

Three-dimensional images are made by stacking sequences of two-dimensional slice images. The slices are tomographic reconstructions from a large number of projection images obtained by the scanning system. The inversion process required to obtain a spatial image from projections uses the filtered back-projection algorithm, see e.g. [15] This algorithm consists of two steps, filtering the projection and back projecting the information on the three-dimensional image volume that represents the scanned sample. The distance from source to target is long relative to the sample size. Therefore, a parallel beam reconstruction is a valid approximation [16]. The setups for the two imaging modalities share this property. For shorter source-to-detector distances, the cone shaped beam geometry must be considered. This is the case for desktop μ -CT scanners. The most common algorithm for cone beam CT reconstruction is the Feldkamp algorithm [17].

During reconstruction, the raw intensity data in the sinogram are converted to CT-numbers or CT-values that have a range determined by the computer system. The most common scale used has been 12-bit [10], in which 4096 values are possible. On most industrial scanners, these values correspond to the grayscale in the image files created or exported by the systems. Although CT values should map linearly to the effective attenuation coefficient of the material in each voxel, the absolute correspondence is arbitrary [10]. Medical systems generally use the Hounsfield Unit (HU), in which air is given a CT number of -1000 and water is given a value of 0. Industrial CT systems are sometimes calibrated so that air has a value of 0, water of 1000, and aluminum of 2700, so the CT number corresponds roughly with density [18].

3.4 Artifacts and partial volume effects

Scanning artifacts such as beam hardening, ring artifact can obscure details of interest or cause the CT values of a single material to change in different parts of the image. Partial-volume effects, if not properly accounted for, can lead to erroneous determinations of feature dimensions and component volume fractions [7].

3.4.1 Beam hardening

Typical for lab based micro-CT is the generation of a polychromatic beam, i.e. a beam that contains a wide spectrum of different X-ray energies. As the beam passes through an object the X-rays low energy are more easily being absorbed, thus depleting the lower energies of the spectrum. So, the general output has a relative higher average energy spectrum. This causes the edges of a tomographic image to be more attenuated [19], shown in Figure 6. The effect of beam hardening on a tomographic image is also called the cupping effect [20]. There are 2 approaches to resolve

this issue. The first approach is to pre filter the beam with a metal plate. This will lower the lowest energy spectrum so later beam hardening will occur less. This method however leads to greater noise on the image [10]. Another method is to process the beam hardening in the post-processing in the reconstruction phase [10].

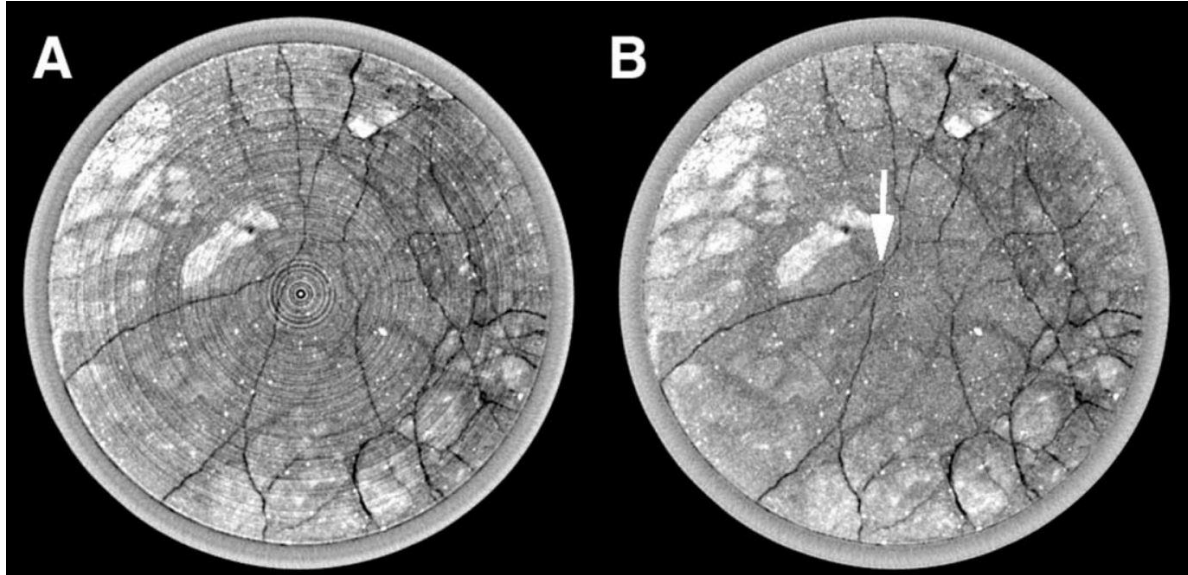


Figure 6

Scans through 15-cm diameter column of saprolite encased in PVC pipe, showing scanning artifacts and software correction. The Scan represent 1-mm thick slice collected with X-ray source at 420kV and acquisition times of 3 min. (A) shows both ring- and beam-hardening artifacts. The former appears as a circular constructions and the latter is visible most obviously as bright ring around outer part of PVC. Image (B) is result of software correction of ring artifacts in (A). From [10]

3.4.2 Ring artifact

Ring artefacts are caused by different outputs of the detectors due to different sensitivity to varying beam hardness. These errors are expressed in the image as circular constructions. Figure 6A. Luckily these artefacts can be overcome with ease through software remedies [10].

3.4.3 Partial volume effect

Each pixel or voxel in a CT image represents the attenuation properties of a specific material volume. This attenuation is the average of the total attenuation of that volume. This causes small properties to get lost in the image, but also gives an opportunity to interpret structures that are smaller than the highest resolution of the CT image [10]. Figure 7. shows us that a voxel can represent one pore space or a representation of different pore space which have a smaller size as the resolution of the voxel.

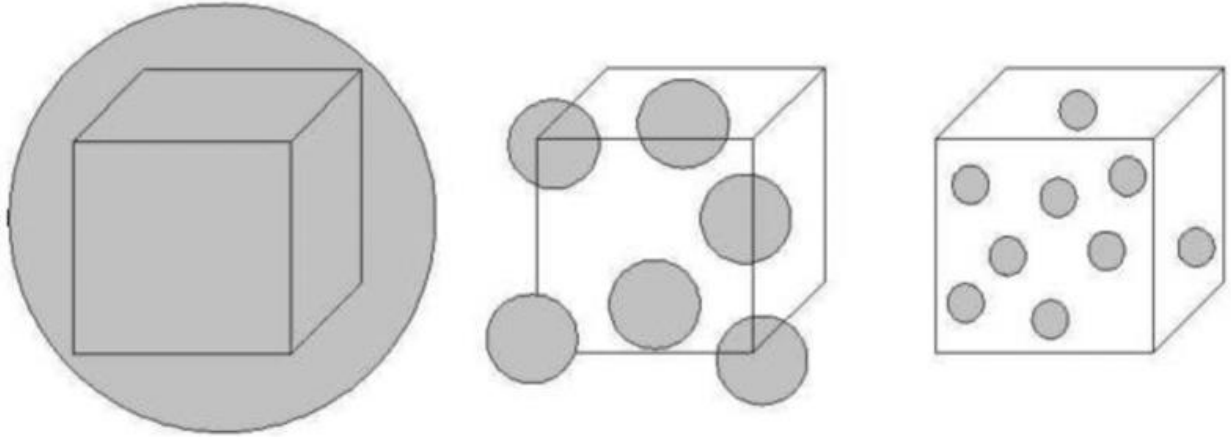


Figure 7

A clarification for partial-volume effect, where the gray spheres represent the pores and the cubes represent the voxel size. A voxel can represent one pore space or different pore space which have a smaller size as the resolution of the voxel. From [21]

3.5 Image enhancement

Images are rarely perfect representations of the attenuation coefficients, since they are disturbed by optical transfer functions, scatter, and noise. In general, the objective of image enhancement is to maximize the contrast between features of interest while minimizing or eliminating artifacts that can interfere with analysis. Consequently, the first operation on an image is usually to apply a filter that reduces the noise level. A smoothing filter, i.e. a filter with low-pass characteristics (a low-pass filter (LPF) is a filter that passes signals with a frequency lower than a selected cutoff frequency and attenuates signals with frequencies higher than the cutoff frequency), generally suppresses the noise. The first filters that one encounters in the image processing literature are convolution filters of different flavors, e.g. Box or Gauss filters [13,20]. Another common approach is to use a median filter that performs especially well with outliers. Both of these filters have low-pass characteristics and are spatially invariant. The effect of such filters is a smoothing that also affects sharp edged features in the image. This smoothing is undesired since it will negatively affect the resolution and the identification of edges. Noise suppression as a part of the tomographic reconstruction has the same effect. There are solutions to the noise suppression problem that smooth regions with essentially constant intensity while maintaining or even sharpening edges such as the non-linear diffusion filter. The original works by Perona and Malik [22]. For the sake of understanding the working principles of filtering algorithms, here, the Median and Gaussian filters will be briefly discussed.

3.5.1 Median filter:

The median filter is a nonlinear signal processing technology based on statistics [23]. The noisy value of the digital image or the sequence is replaced by the median value of the neighborhood (mask). The pixels of the mask are ranked in the order of their gray levels, and the median value of the group is stored to replace the noisy value. In other words, the median filter considers each pixel in the image in turn and looks at its nearby neighbors to decide whether or not it is representative of its surroundings. Instead of simply replacing the pixel value with the mean of neighboring pixel values, it replaces it with the median of those values [23]. The median is

calculated by first sorting all the pixel values from the surrounding neighborhood into numerical order and then replacing the pixel being considered with the middle pixel value. (If the neighborhood under consideration contains an even number of pixels, the average of the two middle pixel values is used.) Figure 8 illustrates an example calculation.

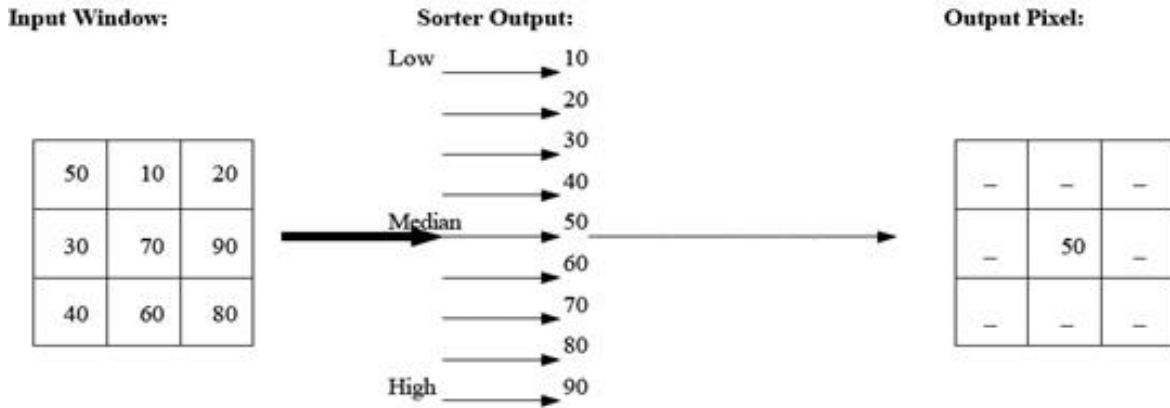


Figure 8
Example Illustrate calculation of Median filter. From [23]

3.5.2 Gaussian filter:

Is the most commonly used filter. It is a linear process. It uses a Gaussian function to calculate each pixel in the image and apply the conversion [24]. Gaussian blur one main objective is to reduce image's high-frequency components [24]. The application of a Gaussian filter is to reduce the noise and reduce detail in the aim of performing better segmentation of the image it is also used as a preprocessing stage.

The Gaussian smoothing operator is a 2-D convolution operator that is used to 'blur' images and remove detail and noise. In this sense it is similar to the mean filter, but it uses a different kernel that represents the shape of a Gaussian ('bell-shaped') hump. This kernel has some special properties. The Gaussian distribution in 1-D has the form:

$$G(x) = \frac{1}{\sqrt{2\pi}\sigma} e^{-\frac{x^2}{2\sigma^2}} \quad \text{Eq (3)}$$

where σ is the standard deviation of the distribution. The distribution is illustrated in Figure 9.

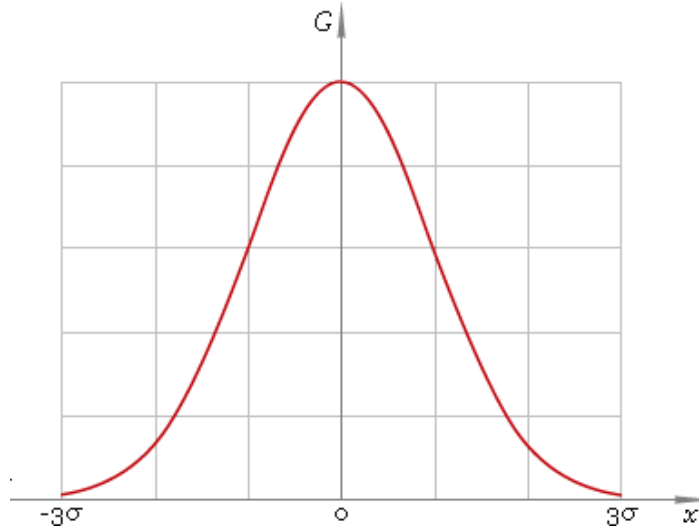


Figure 9

1-D Gaussian distribution with mean 0 and $\sigma=1$.

In 2-D, an isotropic (i.e. circularly symmetric) Gaussian has the form:

$$G(x, y) = \frac{1}{2\pi\sigma^2} e^{-\frac{x^2+y^2}{2\sigma^2}} \quad \text{Eq (4)}$$

This distribution is shown in Figure 10.

In figure 11 an example shows the original image obtained by μ -CT facility and the effect of two different smoothing filtering, Gaussian and Median filters.

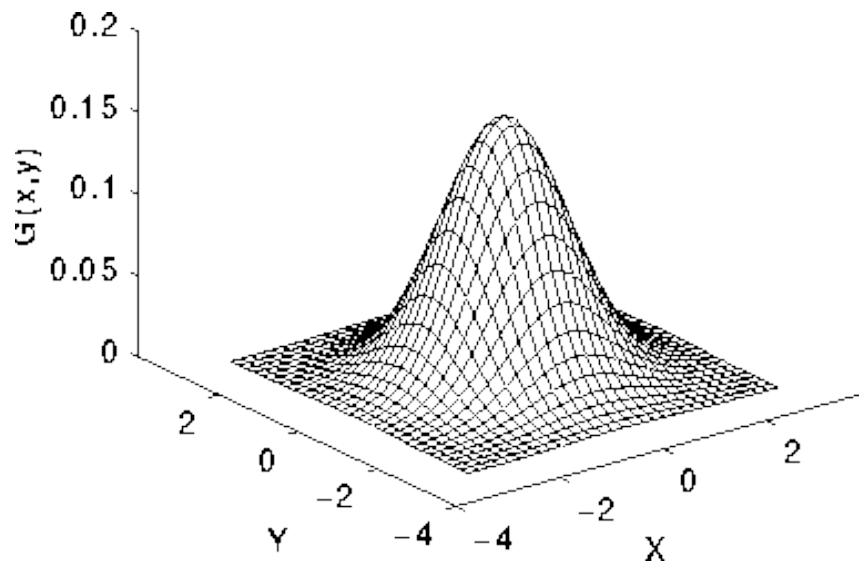


Figure 10

2-D Gaussian distribution with mean (0,0) and $\sigma=1$. From [24]

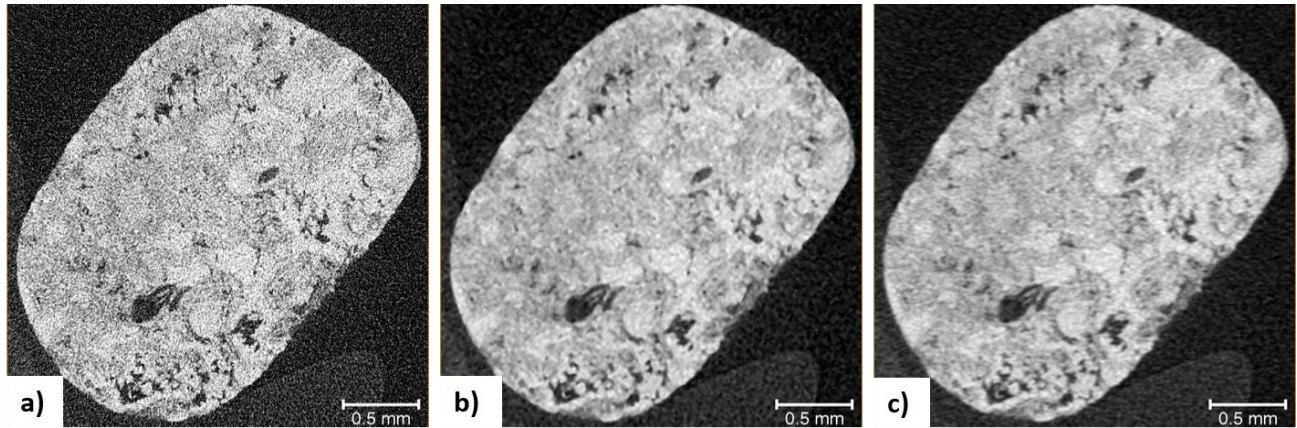


Figure 11

Illustration shows a 2D slice of a carbonate sample obtained by μ -CT the original Image and the resulting Image after the application of different smoothing filters a) Is the original Image without filtering, b) Is the Median filtered image of a) and c) is the Gaussian filtered image of a)

3.6 Segmentation:

The objective of segmentation is to partition an image into regions. We approached this problem by attempting to find boundaries between regions based on discontinuities in intensity levels [13]. The segmentation of an image can be accomplished via thresholds based on the distribution of pixel properties, such as intensity values or color [13]. Segmentation accuracy determines the eventual success or failure of computerized analysis procedures. For this reason, considerable care should be taken to improve the probability of accurate segmentation [13].

Most of the segmentation algorithms are based on one of two basic properties of intensity values: discontinuity and similarity [13]. In the first category, the approach is to partition an image based on abrupt changes in intensity, such as edges. The principal approaches in the second category are based on partitioning an image into regions that are similar according to a set of predefined criteria. Thresholding, region growing, and region splitting and merging are examples of methods in this category. Improvements in segmentation performance can be achieved by combining methods from distinct categories, such as techniques in which edge detection is combined with thresholding [13].

There are various classification schemes for image segmentation methods proposed in literature [25, 26, 27]. A number of methods falling into more than one category. Since information regarding pore shapes and sizes, and the solid matrix structure is usually not available prior to segmentation, texture or shape-based methods are inherently inapplicable for segmentation of pore space and phase distribution in geomaterials [28]. Similarly, the applicability of the watershed method, is generally limited to object detection in well-defined “topographic” data and/or already discretized (binary) images [28].

Here, we will discuss the most popular techniques used for image segmentation which includes, thresholding and region growing.

3.6.1 Thresholding

In thresholding, we can convert a gray-level image into a binary image based on a threshold value as shown in Figure 12. The segmentation threshold value is significant for binary classification, so researchers should choose the appropriate segmentation threshold value carefully. Many studies have shown that different threshold values may lead to different values for pore geometry and topology parameters [29]. There is still no consensus on which type of thresholding method is preferable. For "simple" materials, we can use manual, interactive thresholding method to determine the threshold value, while for high-resolution images, fully-automated segmentation approaches are theoretically enough [30].

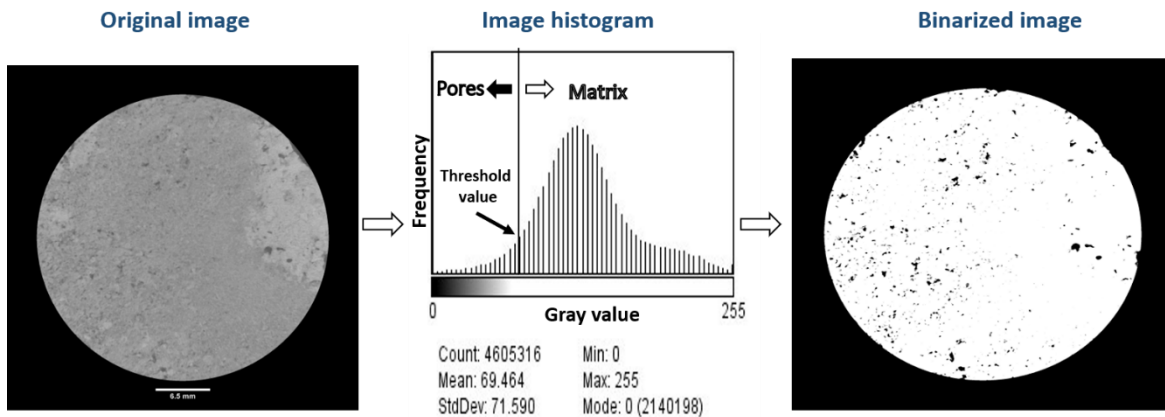


Figure 12

Illustration of histogram based binarization. Left image is a gray scale image the middle image is the image histogram and the right image is the resulted binarized image based on the selected threshold value; where pores appears in black and the matrix appears in white.

3.6.2 Global thresholding

Global thresholding is the most commonly applied approach. A single gray scale value is defined to separate regions of interest on the basis of analysis of the image histogram Figure 12. Depending on the applied approach for selection of the optimal gray scale threshold, global methods may be divided into a number of subcategories. These include methods based on analysis of the histogram shape, correlation between background and foreground pixel entropies, the similarity of attributes between the gray scale and binarized image or higher-order probability distributions and spatial correlations between image pixels [26, 27]

3.6.3 Region growing:

Region growing methods are based on the assumption that all voxels belonging to a particular object are connected and sufficiently similar. A generic algorithm iteratively searches for all voxels neighboring an existing region of interest (ROI) and uses specific selection criteria (commonly the similarity of the neighboring voxels gray scale intensities to the mean intensity of the entire region) to add neighboring pixels to the ROI [13]. Methods within this category mainly differ in applied selection criteria for adding or removing voxels [31] and considerations for local image properties

such as edges [32]. A significant drawback of region growing methods is the need for carefully defining initial seed regions, which is typically done manually or with a conservative use of global thresholding, which limits their applicability to supervised segmentation [33].

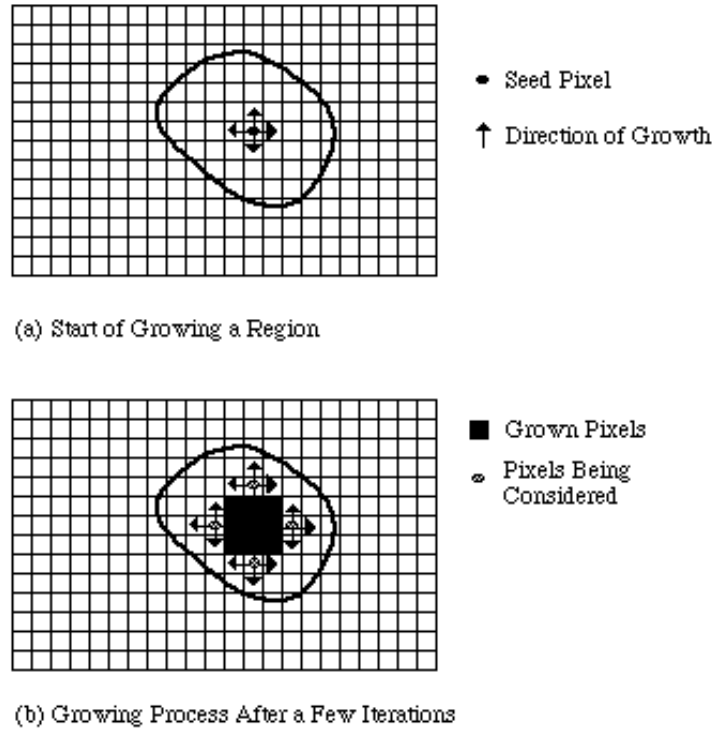


Figure 13
Illustration of region growing based segmentation. From [34]

3.6.4 Hybrid methods

Hybrid methods can be assembled as a combination of various approaches. For example, in certain multiphase systems it may be beneficial to use simple thresholding to remove voxels corresponding to materials with high X-ray attenuation prior to performing precise segmentation of the pore space [35]. Alternatively, one could use region growing or level set methods as an efficient means for refinement of segmentation results obtained with less computationally demanding methods, or obtain optimal segmentation by comparing results of several different algorithms [35].

4. Three-dimensional pore network model extraction (PNM)

After the binarization of the gray level image for isolating the pore space, a binary 3D image of the macro-porous pore space can be obtained and the porosity can be measured. subsequently an equivalent network of the pore and throat type can be build for petrophysical properties calculations. Figure 14 shows the work flow to generate PNM. To a large extent the success of pore network models depends on the way they represent the real pore space in terms of its

geometrical and topological characteristics for a given application. Previous works have clearly demonstrated the importance of the geometric properties of the porous media, such as the locations of pores and throats, the distributions of sizes and shapes of pores and throats [36, 37]. Based on the work of Xiong et al [38] there are three ways to construct a PNM representing a porous medium. The first method is to create a statistically equivalent network using distributions of basic morphologic parameters, while the second approach is to map a network structure directly onto a specific porous medium void space. The fundamental difference between the two methods is that the direct mapping provides a one-to-one spatial correspondence between the porous medium structure and the equivalent network structure, whereas the other type of network is equivalent only in a statistical sense to the modelled system. The last method is called the grain-based approach, which is based on the diagenesis of porous media [38]. Here, two of the direct mapping methods will be briefly illustrated.

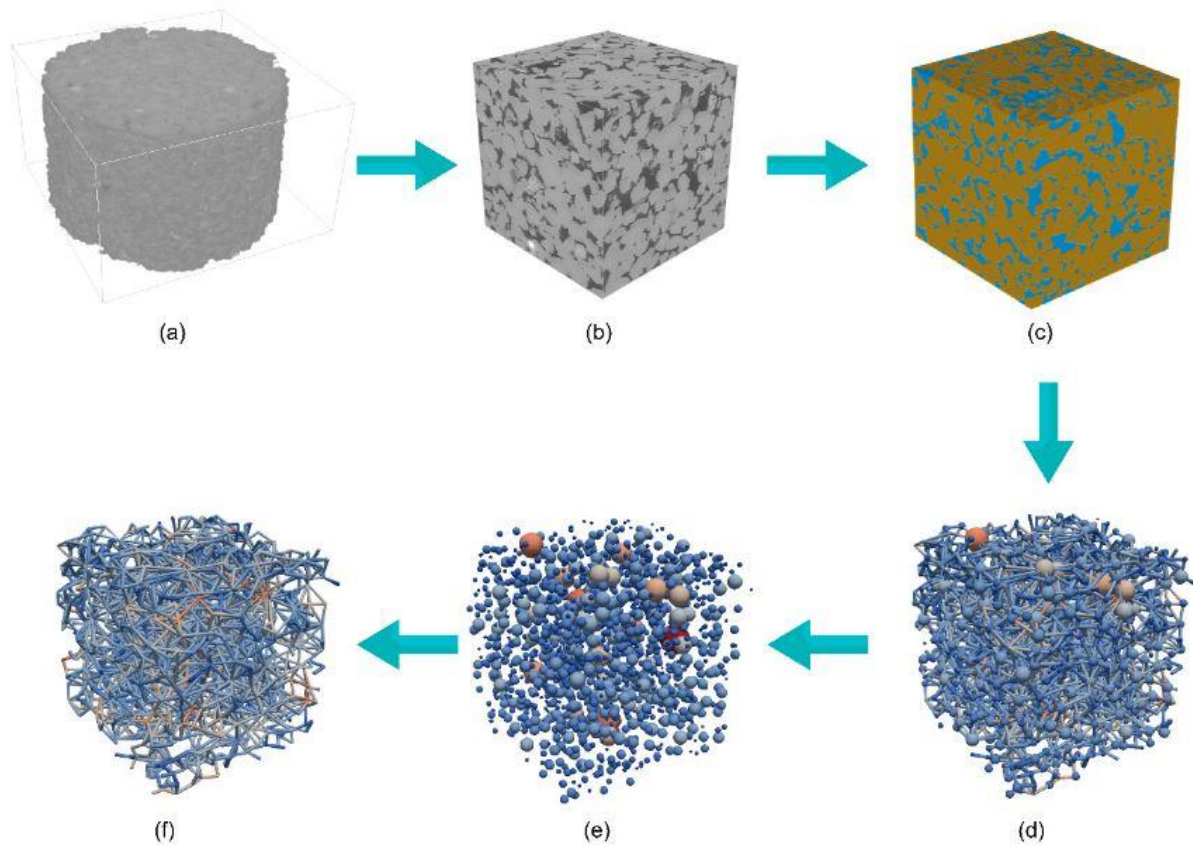


Figure 14

Workflow to generate the pore network model (PNM). (a) The original 3D volume; (b) the sub-volume; (c) the binary sub-volume; (d) the full PNM, including nodes and links; (e) nodes in the PNM; and (f) links in the PNM. From [39]

4.1 Direct mapping model

Based on 3D images, the following approaches have been used to construct irregular pore network models

4.1.1 Medial axis method

The medial axis-based methods transform the pore space images into a medial axis that was the reduced representation of the pore space acting as a topological skeleton as show in figure 15. The topological skeleton is constructed roughly along the middle of the pore channels either by a thinning algorithm [40] or a pore-space pruning algorithm [41]

The medial axis mathematically preserves the topology of the pore space. However, it is difficult to identify pores unambiguously. Furthermore, pores normally encompass more than one junction of the medial axis; therefore, various merging algorithms have to be developed to trim the skeleton and fuse the junctions together while avoiding unrealistically high coordination numbers [42]. In Figure 16 an illustration of the pore network extracted using the medial axis algorithm.

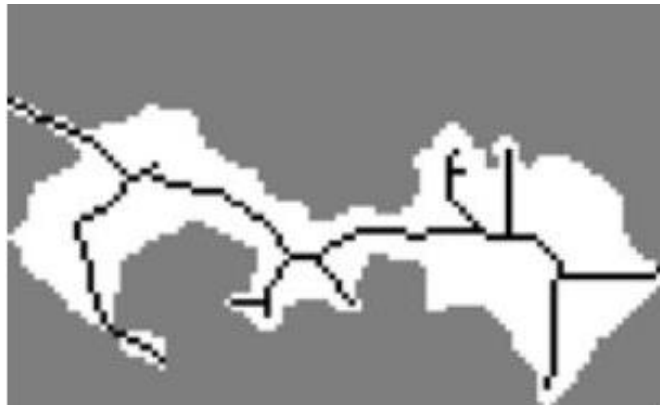


Figure 15

(a) Initial skeleton of the pore space, where the channel is generally described by a single line while the pores, on the contrary are described by a group of lines and vertices. [43].

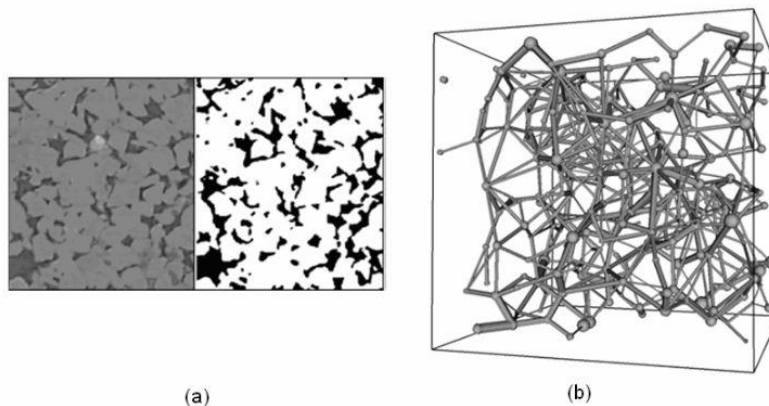


Figure 16

(a) shows the gray scale and segmented images of a sandstone; (b) is the network of this sandstone pores extracted using the medial axis algorithm. From [44]

4.1.2 The maximal ball method

The maximal ball algorithm also denoted as MB [45, 46] starts from each voxel in the pore space to find the largest inscribed spheres that just touch the grain or the boundary, Figure 17. Then those included in other spheres are viewed as inclusions and removed; the rest are called maximal balls and describe the pore space without redundancy. Locally the largest maximal balls identify pores while the smallest balls between pores are throats. The maximal balls were used in Silin's work 2003 and 2006 [45, 46] mainly for calculating the dimensionless capillary pressures for the pore space rather than to extract a pore network from the image. A MB must touch the grain surface and so MBs cannot be a subset of any other MB. Therefore, every MB is in possession of at least one voxel that is not contained in any other MB. The aggregate of all MBs defines the void space in a rock image without redundancy.

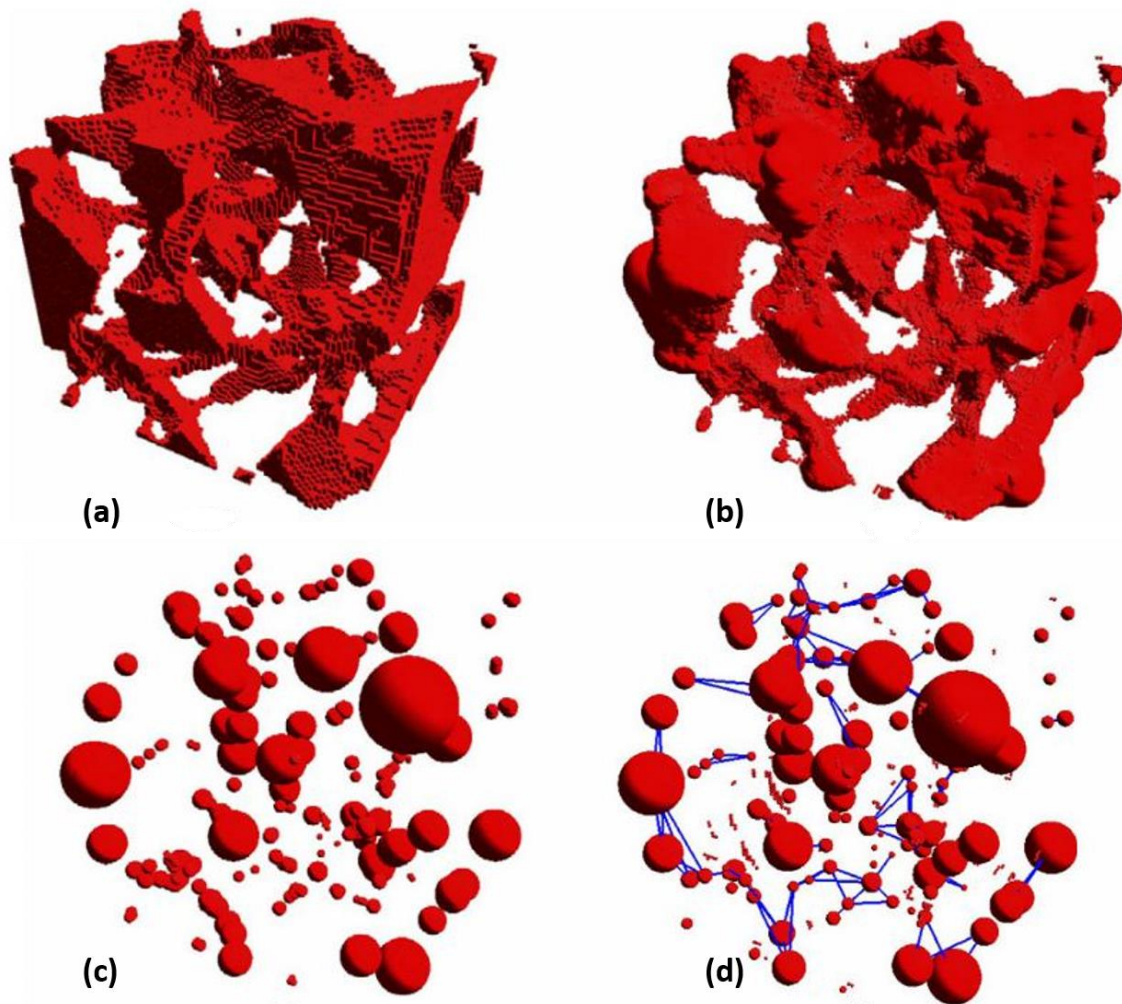


Figure 17

(a) is the pore space image of a Fontainebleau sandstone with a porosity of 17%; (b) is maximal balls in the pore space. The dimensionless sizes of the images are $200 \times 200 \times 200$ counted in voxels; (c) shows master balls (pores) found in (a); (d) is the pores and their connectivity of the pore space. From [44]

5. CONCLUSIONS

The aim of this work is to present the possibilities of X-Ray computed tomography in determination of petrophysical parameters of reservoir rocks. On the basis of literature it has been confirmed that X-Ray microtomography is at present one of the best and most modern research methods used by geologists and petrophysics. This method enables visualization of the internal structure of the rock, helping to understand the petrophysical properties of the reservoir rocks, and allowing to simulate the flow phenomena of different fluid reservoirs in the rock pore space [9]. Most of the research results, estimated by the microtomography method, were consistent with the results of laboratory tests, indicating its accuracy [9]. Computed tomography and Image processing techniques also give the possibility to measure the porosity, permeability, oil and gas saturation, capillary pressure, wettability, electrical and elastic parameters of reservoir rocks [9].

References

- [1] Petrovic, J.E., Siebert, P.E. 1982. Rieke Soil bulk-density analysis in 3 dimensions by computed tomographic scanning. *Soil Science Society of America Journal*, 46 (3) (1982), pp. 445-450.
- [2] Hainsworth, J., Aylmore, L. 1983. The use of computer assisted tomography to determine spatial distribution of soil water content. *Aust J Soil Res*, p. 435.
- [3] ARNOLD, J.R., TESTA, J.P.J., FRIEDMAN, P.J., KAMBIC, G.X. 1982. Computed tomographic analysis of meteorite inclusions. *Science*, 219, 383-384.
- [4] VINEGAR, H.J. 1986. X-ray CT and NMR imaging of rocks. *Journal of Petroleum Technology*, 38, 257-259.
- [5] HAUBITZ, B., PROKOP, M., DOHRING, W., OSTROM, J.H., WELLNHOFER, P. 1988. Computed tomography of Archeopteryx. *Paleobiology*, 14, 206-213.
- [6] KENTER, J.A.M. 1989. Applications of computerized tomography in sedimentology. *Marine Geotechnology*, 8, 201-211.
- [7] Wellington, S.L., Vinegar, H.J. 1987. X-ray computerized tomography. *Journal of Petroleum Technology*, 39 (8), 885–898.
- [8] Herman, G. T. 2009. *Fundamentals of computerized tomography: Image reconstruction from projection*, 2nd edition, Springer, p. 300.
- [9] Kułynycz, V., Maruta, M. 2017. The application of X-Ray Computed Microtomography for estimation of petrophysical parameters of reservoir rocks. *World Scientific News*, 76, 91–107. www.worldscientificnews.com.
- [10] Richard, A., Ketcham., William, D., Carlson. 2001. Acquisition, optimization and interpretation of X-ray computed tomographic imagery: applications to the geosciences, *Computers & Geosciences* 27, 381–400.
- [11] Silver, M.D. 1994. Target self-attenuation extension to the Desorby and Boyer thick-target bremsstrahlung spectrum. *Medical Physics* 21 (4), 577–579.
- [12] Markowicz, A.A. 1993. X-ray physics. In: Van Grieken, R.E., Markowicz, A.A. (Eds.), *Handbook of X-ray Spectrometry*. Marcel Dekker, New York, pp. 1–28.
- [13] Gonzalez, R., Woods, R. 2008. CV book. In *Digital Image Processing: Vol. 3rd Edition (Issue 3)*. P. 943.

- [14] Zinsmeister, W.J., De Nooyer, C. 1996. Computed tomography; non-destructive techniques for visualizing internal morphology of invertebrates. Geological Society of America, Abstracts with Programs 28 (7), 294.
- [15] Kak, A., Slaney, M. 1988. Principles of computerized tomographic imaging. IEEE Press.
- [16] Kaestner, A., Lehmann, E., Stampanoni, M. 2008. Imaging and image processing in porous media research. *Advances in Water Resources*, 31(9), 1174–1187. <https://doi.org/10.1016/j.advwatres.2008.01.022>.
- [17] Feldkamp, L., Davis, L., Kress, J. 1984. Practical cone-beam algorithm. *J Opt Soc AmA*;1(6):612–9.
- [18] Johns, R.A., Steude, J.S., Castanier, L.M., Roberts, P.V. 1993. Nondestructive measurements of fracture aperture in crystal- line rock cores using X-ray computed tomography. *Journal of Geophysical Research* 98 (B2), 1889–1900.
- [19] Wildenschild, D., Sheppard, A.P. 2013. Advances in Water Resources X-ray imaging and analysis techniques for quantifying pore-scale structure and processes in subsurface porous medium systems. *Advances in Water Resources*, 51, pp.217–246.
- [20] Cnudde, V., Boone, M.N. 2013. High-resolution X-ray computed tomography in geosciences: a review of the current technology and applications, *Earth Science Reviews*, doi: <http://dx.doi.org/10.1016/j.earscirev.2013.04.003>.
- [21] Cnudde, V. 2005. Exploring the potential of X-ray tomography as a new non-destructive research tool in conservation studies of natural building stones.
- [22] Perona, P., Malik, J. 1990. Scale-space and edge detection using anisotropic diffusion. *IEEE Trans Pattern Anal Mach Intell*;12(7):629–39.
- [23] Kwame, B., Benjamin, W., David, S. 2012. Improving the Effective ness of the Median Filter. *International Journal of Electronic and Communication Engineering*; ISSN 0974-2166; 5(1): 85-97.
- [24] Xin, s., Song, Q., Yang, L., Jia, W. 2016. "Recognition of the smart card iconic numbers", *Proc. Int. Conf. Electron. Inf. Comput. Eng.*, vol. 44.
- [25] Haralick., Robert, M., Linda, G. 1992. *Computer and Robot Vision, Volume I*. Addison-Wesley. P.
- [26] Pal, N.R., Pal, S.K. 1993. A review on image segmentation techniques. *Pattern Recognition*, 26, 1277–1294. doi:10.1016/0031-3203(93)90135-J.
- [27] Sezgin, M., Sankur, B. 2004. Survey over image thresholding techniques and quantitative performance evaluation. *Journal of Electronic Imaging*, 13, 146–165. doi:10.1117/1.1631315.

- [28] Iassonov, P., Gebrenegus, T., Tuller, M. 2009. A crucial step for characterization and quantitative analysis of pore structures. *Water Resources Research*, 45(9), 1–12.
<https://doi.org/10.1029/2009WR008087>.
- [29] Baveye, P.C., Laba, M., Otten, W., Bouckaert, L., Sterpaio, P.D., Goswami, R.R., Grinev, D., Houston, A., Hu, Y., Liu, J. 2010. Observer-dependent variability of the thresholding step in the quantitative analysis of soil images and X-ray microtomography data. *Geoderma*, 157, 51–63.
- [30] Porter, M.L., Wildenschild, D. 2010. Image analysis algorithms for estimating porous media multiphase flow variables from computed microtomography data: A validation study. *Comput. Geosci*, 14, 15–30.
- [31] Wirjadi, O. 2007. Survey of 3D Image Segmentation Methods, Technical report No. 123 vol. 35.
- [32] Vlidis, T., Liow, Y.-T. 1990. Integrating region growing and edge detection, *IEEE Trans. Pattern Anal. Mach. Intel.*, 12, 208–214.
- [33] Iassonov, P., Gebrenegus, T., Tuller, M. 2009. Segmentation of X-ray computed tomography images of porous materials: A crucial step for characterization and quantitative analysis of pore structures. *Water Resources Research*, 45(9), 1–12.
<https://doi.org/10.1029/2009WR008087>.
- [34] Xiaoli, Z., Xiongfai, L., Yuncong, F. 2015. A medical image segmentation algorithm based on bi-directional region growing, *Optik*, 126, 20, Pages 2398-2404.
- [35] Melgani, F. 2006. Robust image binarization with ensembles of thresholding algorithms, *J. Electron. Imaging*, 15(2), doi:10.1117/1.2194767.
- [36] Blunt, M.J., King, M.J., Scher, H. 1992. Simulation and theory of two-phase flow in porous media. 20, pp. 77–103.
- [37] Oren, P.-E. 1994. Pore-scale network modelling of water flood residual oil recovery by immiscible gas flooding. *SPE/DOE Improved Oil Recovery Symposium*.17–20.
- [38] Xiong, Q., Baychev, T. G., Jivkov, A. P. 2016. Review of pore network modelling of porous media: Experimental characterizations, network constructions and applications to reactive transport. *Journal of Contaminant Hydrology*, 192, 101–117.
<https://doi.org/10.1016/j.jconhyd.2016.07.002>.
- [39] Gong, L., Nie, L., Xu, Y. 2020. Geometrical and topological analysis of pore space in sandstones based on x-ray computed tomography. *Energies* 13(15).

- [40] Baldwin, C.A., Sederman, A.J., Mantle, M.D., Alexander, P., Gladden, L.F. 1996. Determination and characterization of the structure of a pore space from 3D volume images. *J. Colloid Interface Sci.* 181 (1), 79–92.
- [41] Lindquist, W.B., Lee, S.M., Coker, D.A., Jones, K.W., Spanne, P. 1996. Medial axis analysis of void structure in three-dimensional tomographic images of porous media. *J. Geophys. Res. Solid Earth* 101 (B4), 8297–8310 (1978–2012).
- [42] Jiang, Z., Wu, K., Couples, G., van Dijke, M., Sorbie, K., Ma, J. 2007. Efficient extraction of networks from three-dimensional porous media. *Water Resources*. 43 (12).
- [43] Youssef, S., Rosenberg, E., Gland, N., Bekri, S., Vizika, O. 2007. Quantitative 3D Characterization of the Pore Space of Real Rocks : Improved M -Ct Resolution and Pore Extraction Methodology. *International Symposium of the Society of Core Analysts, September 2015*, 1–13.
- [44] Dong, H., Blunt, M. J. 2007. Micro-CT imaging and pore network extraction. *Earth Science and Engineering*, 217.
- [45] Silin, D.B., Jin, G., Patzek, T.W. 2003. Robust Determination of Pore Space Morphology in Sedimentary Rocks, *J Petrol Technol.* 56, pp. 69-70.
- [46] Silin, D., Patzek, T. 2006. Pore space morphology analysis using maximal inscribed spheres. *Physica A*, 371: 336-360.